Impact of ionization peak location on measured opaqueness in DIII-D H-mode plasmas

J.J. Balbin-Arias[1], S. Mordijck[1], T.M. Wilks[2], L. Horvath[3], T. Odstrcil[4], R.A. Chaban[1], A.M. Rosenthal[2,5], J.W. Hughes[2], A. Bortolon[3], F.M. Laggner[6], R. Gerrú[2]

[1] William & Mary, Williamsburg, VA 23187, USA
[2] PSFC MIT, Cambridge, MA, USA
[3] Princeton Plasma Physics Laboratory, NJ, USA
[4] General Atomics, PO Box 85608, San Diego, California 92186–5608, USA
[5] Commonwealth Fusion Systems, MA, USA
[6] North Carolina State, Raleigh, NC, USA

E-mail: jjbalbinarias@wm.edu

Abstract.

This study investigates the relationship between electron pedestal density and the location of the ionization peak on neutral penetration in DIII-D H-mode plasmas, utilizing a database of Lyman-α emission measurements. The high electron density leads to neutrals being "screened" and the ionization front being pushed out into the Scrape-Off Layer (SOL). This is also referred to as the neutral opaqueness, which is heuristically expected to scale with edge plasma density and machine size. However, at lower electron pedestal density, the penetration depth of the neutrals varies, and measured opaqueness deviates from the heuristic scaling. The database reveals that at low density, when the ionization peak is located in SOL region, the linear relationship between the electron density and neutral penetration holds. However, when the peak is located inside the separatrix, the penetration of the neutrals (λ_{n_0}) is much wider $\sim 3.0 - 3.5$ cm, breaking the heuristic opaqueness approximation. These findings provide valuable insights into fueling efficiency and plasma behavior, with implications for Fusion Pilot Plants (FPPs) where high pedestal densities are anticipated and where the neutral opaqueness behaves like its heuristic approximation. This analysis offers a framework to refine neutral opaqueness approximations, enhancing the predictive capability for advanced tokamak operations.

1. Introduction

Understanding neutral penetration and its impact on the electron pedestal density structure is essential for optimizing the performance of Fusion Pilot Plants (FPPs). These devices will need to achieve high plasma density and excellent energy confinement, as outlined by the Lawson criterion, to sustain fusion reactions. A key challenge is that those densities in the pedestal region significantly reduce neutral penetration past the

separatrix, creating a highly "opaque" plasma edge. This paper investigates how the relative location of the ionization peak with respect to the pedestal foot correlates with the electron density at the top of the pedestal, and how this influences the penetration of neutrals past the separatrix. The analysis is based on a database of DIII-D H-mode plasmas with direct Lyman- measurements. To quantify the penetration of neutrals relative to the pedestal scale, we compare the pedestal width of the electron density profile (Δ_{n_e}) with the characteristic exponential decay length of the neutral density profile (λ_{n_0}). This comparison yields the experimental opaqueness parameter, defined as $\eta = \Delta_{n_e}/\lambda_{n_0}$.

The opaqueness in current-day tokamaks is about 5-10 lower than the values expected from ITER ($\sim 1.2 \times 10^{20} m^{-2}$), estimating the opaqueness like $a(n_{e,SEP} + n_{e,PED})/2$, being a the minor radius, $n_{e,SEP}$ and $n_{e,PED}$ the electron density at the separatrix and the pedestal, respectively [1,2]. This means that in current-day devices, a change in fueling has a direct effect on the pedestal density structure. In addition, the protection of metal walls requires detached divertor conditions, which currently results in high divertor neutral densities and directly affect the pedestal density structure in open divertor configurations [3, 4]. The high neutral densities leak from the divertor to the x-point, which leads to a strong asymmetry in the neutral density not just in the SOL, but also inside the separatrix. However, in FPP devices where the divertor legs will be much more opaque, due to higher edge electron densities and temperatures, the neutrals will be trapped in the divertor region. This can be further enhanced by designing devices with advanced closed divertor configurations. As a result, the impact of neutral poloidal asymmetries on the pedestal structure will be diminished in FPPs, but cannot be ignored in current day devices [5].

The impact of neutrals on the pedestal density structure has been mostly studied using a variety of models. This is linked to the challenges associated with measuring neutral densities in tokamaks. Most devices rely on Balmer-α measurements to determine the ionization levels. The analysis of Balmer-α light to extract neutral atomic densities is complicated by reflections and molecular contributions [6–8]. DIII-D circumvents these limitations by using the Lyman-α emission spectrum similar to Lyman-α measurements which were pioneered with the LYMID diagnostic on C-Mod [9]. The DIII-D Lyman Alpha Measurement Apparatus (LLAMA) diagnostic takes this a step further by measuring the ionization both on the High Field Side (HFS) and Low Field side (LFS) [6].

With measurements on both the HFS and LFS, we can investigate the influence of asymmetries in ionization and neutral densities. Previous research on ASDEX Upgrade and JET showed the formation of a high-density region on the HFS (HFSHD), which directly affected the fueling source and the pedestal density structure. An outward shift of the electron density pedestal with respect to the electron temperature pedestal is observed, which in turn strongly affects the stability and pedestal performance [10–12]. Initial dedicated measurements using the LLAMA diagnostics have indicated that the neutral density on the HFS is an order of magnitude larger than on the LFS and that

the neutral penetration depth can vary substantially [13]. In DIII-D this asymmetry depends on the direction of the grad-B drift direction and the balance of particle fluxes to the inner versus outer divertor respectively [14]. As LLAMA measures both the HFS and LFS ionization rate profiles, the asymmetry between the two sides can be included in a qualitative description of the difference of their neutrals profiles, and their penetration depth as a function of an H-mode database.

Previously, C-Mod experimental measurements along with KN1D and SOLPS-ITER modeling has shown that neutral penetration is reduced by enhancing the electron pedestal density [2, 15, 16]. In addition, the impact of isotope mass on neutral penetration revealed a dependence on the square root of the mass ratio in DIII-D H-mode plasmas [13]. These studies showed that altering the electron density in given machine, for a given magnetic configuration provides a direct means of altering the opaqueness of the plasma to neutrals. The definition of neutral opaqueness, $\eta = \Delta_{\mathrm{n_e}}/\lambda_{\mathrm{n_0}}$ is expressed as the relative level of penetration of neutrals, $\lambda_{\mathrm{n_0}}$ with respect to the pedestal electron density width $\Delta_{\mathrm{n_e}}$ [1]. This neutral opaqueness (η) is analogous to the opaqueness of light incident on a medium [2]. This assumes that the neutral density inside the separatrix can be approximated by an exponential function, being the exponential decay length obtained at the separatrix position. This parameter is known as the neutral penetration depth $\lambda_{\mathrm{n_0}}$. This approximation has been shown to be a good assumption in H-mode experiments based on the LLAMA measurements in DIII-D and SOLPS-ITER modeling [2, 13]. As neutral measurements and/or simulations results are scarce, a heuristic model was developed, which is not dimensionless, $\eta \sim a\sqrt{A}(\mathrm{n_{e,SEP}} + \mathrm{n_{e,PED}})/2$ [5, 13], with a the minor radius, A the mass ratio of the main ion species with respect to hydrogen, $\mathrm{n_{e,PED}}$ the pedestal electron density, and $\mathrm{n_{e,SEP}}$ the separatrix electron density determined by a power balance method described in [17].

In this paper, we will compare the direct measured opaqueness using the LLAMA diagnostic on both the HFS and LFS and compare these measurements with the heuristic model to better understand its limitations and application. In Section 2 the operational characteristics of the database are introduced. Section 3 describes the methods to determine the pedestal structure and neutral measurements for the database. In section 4 the measured opaqueness is compared to the heuristic model and we show that the location of the ionization peak with respect to the separatrix has a strong influence on the agreement. The discussion in section 5 provides further context on the importance of describing opacity as a function of the ionization peak position at the plasma edge, along with insights into its impact on future fusion pilot plans (FPP).

2. Database

2.1. Operational parameter space

A collection of 39 deuterium DIII-D H-mode discharges with LLAMA measurements was assembled, comprising 686 samples under steady-state conditions (see section 2.3). To

DIII-D	I_P	B_T	q_{95}	P_{NBI}	β_N	W_{DIA}	ν_e^*	$H_{98}(y,2)$	gas A	gas B
	(MA)	(T)		(MW)		MJ			TorrL/s	TorrL/s
Min.	0.97	1.87	3.18	3.02	1.45	0.53	0.30	0.86	0.0	0.0
Max.	1.77	2.15	6.35	12.95	3.21	1.88	4.37	1.83	59.65	92.06

Table 1: DIII-D operational parameters for H-mode database to study ionization and fueling.

limit introducing known poloidal asymmetry changes in neutral behavior the database only includes lower single-null configuration. Besides, the discharges are under the conditions of a toroidal magnetic field (B_T) of approximately $\sim 1.87-2.15$ (T), and with the ion $\nabla B \times B$ drift direction towards the lower X-point. In addition, all discharges with additional impurity and pellet injection have been excluded as both alter the electron density profile and introduce an additional unknown factor in understanding fueling based on ionization from recycling and gas puffing.

Within these limitations we do not impose any restrictions on other operational choices and this did result in a database with a wide range of plasma currents $I_P \sim 0.97 - 1.77$ MA resulting in a wide range of safety factors at the 95% poloidal flux surface, $q_{95} \sim 3.18 - 6.35$, see table 1. None of the H-mode plasmas with LLAMA measurements had ECH heating, so the database only includes Neutral Beam Injected (NBI) heated plasmas. Thus the NBI power ranged $P_{NBI} \sim 3.02 - 12.95$ MW. This resulted in a variation of the normalized pressure $\beta_N \sim 1.45 - 3.21$, the stored energy from diamagnetic loop $W_{DIA} \sim 0.53 - 1.88$ (MJ), the collisionality on the pedestal top $\nu_e^* \sim 0.30-4.37$, and the confinement enhancement factor ranges $H_{98}(y,2) \sim 0.86-1.83$.

In addition gas puffing is employed to vary the electron density with values of $0 - 92$ TorrL/s. The additional gas puffing along with the spread in plasma current, NBI heating allowed for a variation in the pedestal density by a factor 5, which is equivalent to a change in the heuristic opaqueness by a factor 5 as there was no isotope variation, nor any substantial changes in the minor radius of the plasmas. The electron pedestal density varied by $n_{e,PED} \sim 2.77 - 10.32 \times 10^{19} m^{-3}$, the Edge Localized Modes (ELMs) considered are type-I and the z_{eff} is assumed to be ~ 2.5 (not measured).

2.2. Diagnostic determined shape parameters

To study the impact of ionization and neutrals on the electron pedestal density structure, we require diagnostics to measure both the neutrals as well as the electron density. The electron density profiles are measured by the Thomson Scattering (TS) diagnostic as it is illustrated in Figure (1). This provides vertical profiles of electron density and temperature with a radial resolution on the pedestal of $\Delta r \sim 1$(cm) and a temporal resolution of $\Delta t \sim 2.5 - 5.0$ (ms).

The neutral density measurements are inferred from the brightness of the alpha decay in the Lyman band and the measurements of electron density and temperature

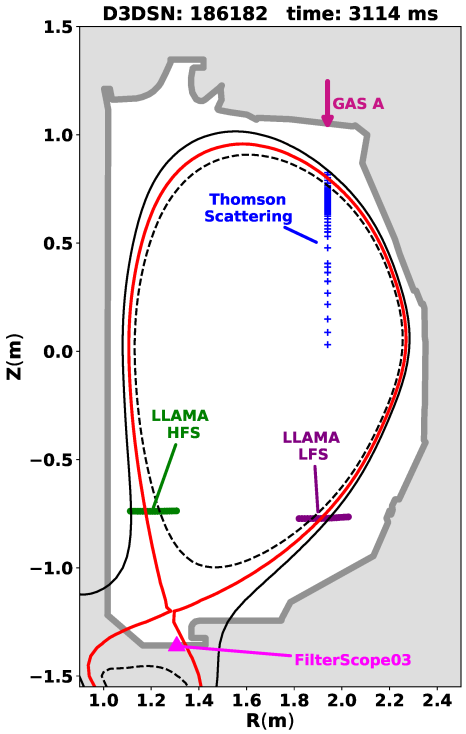

Figure 1: Poloidal profile of the DIII-D shot number 186182 @ t = 3114ms. The current magnetic configuration is chosen to be the most similar magnetic configuration for all the time slices considered in this database.

(see Equation 7). This brightness is measured by harnessing the diagnostic Lyman Alpha Measurements Apparatus (LLAMA) [6]. The LLAMA diagnostic is used to take measurements at a fixed vertical position ($z \sim -0.738\,(\mathrm{m})$) over two radial ranges: one for High Field Side (HFS) at major radius coordinate $R \sim 1.11 - 1.30\,\mathrm{m}$ (*green line)* and one for Low Field Side (LFS) $R \sim 1.82 - 2.02\,\mathrm{m}$ (*purple line),* see figure 1. In a lower single null plasma, the LLAMA array is placed vertically between the mid-plane and the X-point, which in DIII-D coincides with the dominant fueling source location [5].

As both diagnostics have fixed locations in the vacuum vessel, the proper overlapping between the measurement views and the pedestal region is affected by plasma shaping. The LLAMA line of sights on both the HFS and LFS as well as TS coverage of the pedestal and the SOL are crucial. For that reason, all plasmas considered exhibit similarly shaped features (elongation $\kappa \sim 1.69 - 1.81$, lower triangularity $\delta_{lower} \sim 0.19 - 0.39$, and squareness $s \sim 0.33 - 0.39$), as indicated in Figure (2).

Additionally, for the majority of discharges the position of the outer striking point is close to the cryopump entrance, which allows for precise control of the density [13]. The location of the outer strike point was determined using the equilibrium reconstruction provided by EFIT, which solves the Grad-Shafranov equation to determine the magnetic flux surfaces, including the separatrix that defines the boundary of the confined plasma. The precise location of the outer strike point is identified by tracing the magnetic field

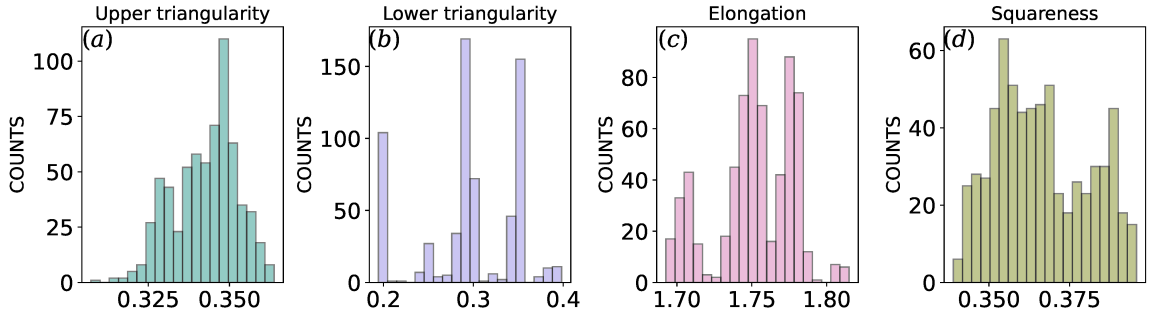

Figure 2: This figure summarizes the shaping parameters to ensure that the magnetic configuration remains largely unchanged across all discharges considered in this database, allowing us to neglect the impact of most of the shaping parameters and the effect from the lower triangularity is considered out of scope of this work.

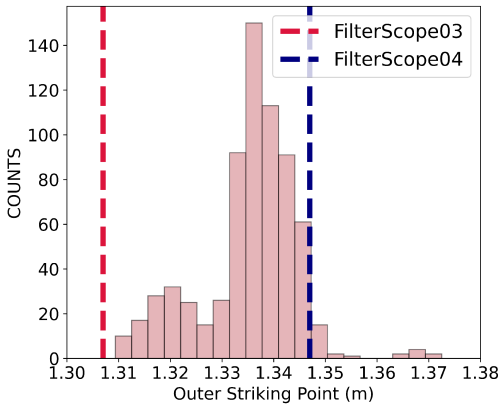

Figure 3: Distribution of the outer strike point relative to the position of the Filter Scopes. Determining the proximity of the outer strike point to a specific Filter Scope helps in filtering ELMs by enabling the identification of ELM sequences in the signal with high resolution.

lines from the separatrix to their intersection with the divertor surface. The majority of the data puts the strikepoint location between $R = 1.33$ to $R = 1.34$ m. The strikepoint location affects the connection to the cryopump and the pumping efficiency. It also affects the openness of the divertor and the ability of the neutrals to escape the divertor region and directly fuel the main plasma.

2.3. Steady-state requirements

To avoid introducing bias due to slow and or fast changes in plasma confinement, we apply two filters to only include steady-state conditions. First, on DIII-D the typical energy confinement is $\tau_{\mathrm{E}} \sim 100\,\mathrm{ms}$ [18]. Particle confinement however has been estimated using particle balance studies on ASDEX to be $\tau_{\mathrm{P}} \sim 3 \times \tau_{\mathrm{E}}$ [19, 20]. As

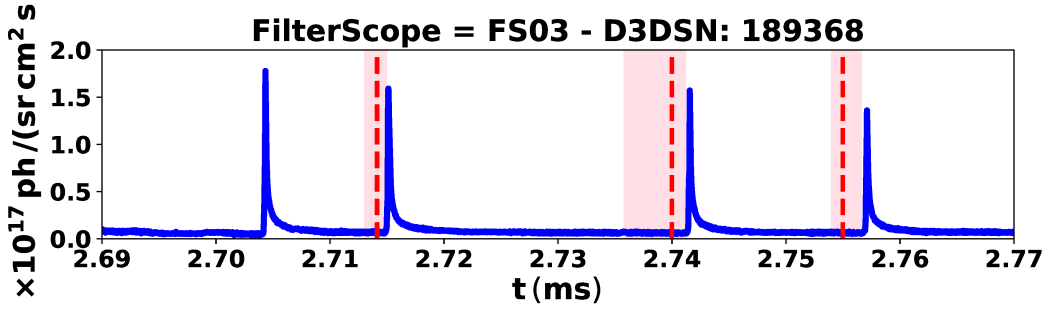

Figure 4: Divertor FilterScope signal FS04 (blue line) used to identify ELMs. The shaded pink regions represent the 80–90% inter-ELM phase. The dashed red lines indicate Thomson Scattering time slices that fall within this intern-ELM time windows. All time slices meeting this criterion form the basis of this database.

a result, the database only includes time windows where the profiles accomplish the steady-state conditions for $\tau_{\mathrm{P}} \sim 3 \times \tau_{\mathrm{E}} \sim 300\,\mathrm{ms}$. This avoids the initial slow time evolutions due to for example changes in injected power and/or gas and focusing on a time window when the plasma has reached a steady-state.

The second filter is in place to remove the contributions of type-I Edge Localized Modes (ELMs). ELMs lead to a fast reduction in pedestal characteristics as the pedestal reaches the peeling-ballooning stability limit. After the ELM crash, the pedestal rebuilds quickly in the early inter-ELM phase, with the electron temperature recovering faster than the electron density. However, by the time we reach the 80% of the inter-ELM cycle, both pedestal values have saturated. To identify the timing of ELMs and define inter-ELM phases, we use the FilterScope diagnostic [21], which measures visible line emission (e.g., D_α, C-III) from the plasma edge using narrow-band interference filters and high-speed photomultipliers. The system provides high temporal resolution (up to 100 kHz) and multiple poloidal viewing chords, allowing reliable identification of ELM onset and inter-ELM recovery phases. In this study, FilterScope channel FS03 and/or FS04, viewing the "Floor" for LSN configuration, is used to identify the start and end of ELMs. The database only considers measurements taken during $80-99\%$ of the inter-ELM phase, as illustrated in Figure 4. While, larger windows could be considered, this prudent choice is applied regularly to H-mode analysis on DIII-D to avoid the recovery process after an ELM burst [13, 18].

3. The pedestal structure and the inference of neutral measurements

The database requires synthesized information on the electron density pedestal characteristics and the neutral density. This section describes the process for determining the fits made to the electron density pedestal using the Thomson Scattering diagnostic as well as fits to the neutral density measurements from the LLAMA diagnostic.

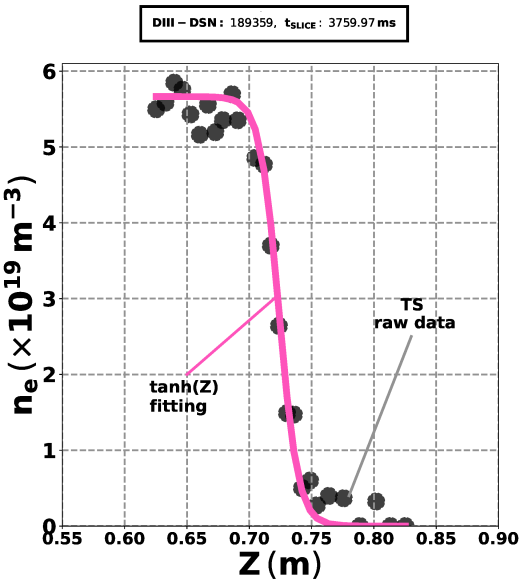

Figure 5: Thomson Scattering vertical profile (associated with the Z-coordinate) of the electron density (black dots) fitted with a tanh function (pink curve) to extract information about the pedestal density structure.

3.1. Electron Pedestal density and its characterization

It is important to note that the *"pedestal"* is a significant feature of the radial electron density profile in a tokamak operating in H-mode [22]. The shape of the pedestal is often fitted with a tanh function, to extract quantities related to the pedestal height and width [15, 18, 23, 24]. These quantities allow to synthesize the pedestal structure necessary for database comparison. Each Thomson scattering time slice is fitted using the following function:

$$f(r) = \mathrm{n_{e,base}} + \frac{\mathrm{n_{e,PED}} - \mathrm{n_{e,base}}}{2}\left[\tanh\left(\frac{2\Delta \mathrm{r}}{\Delta \mathrm{n_e}}\right) + 1\right] + m\left(\Delta r - \Delta \mathrm{n_e}/2\right) \times \mathcal{H}\left(\Delta r - \Delta \mathrm{n_e}/2\right).$$

Here, $\Delta_{\mathrm{n_e}}$ and $\mathrm{n_{e,PED}}$ represent the pedestal width and height, respectively, while $\mathrm{n_{e,base}}$ denotes the base value of the tanh function. The quantity $\Delta \mathrm{r} = \mathrm{r_{sym}} - \mathrm{r}$ corresponds to the difference between the symmetry point $\mathrm{r_{sym}}$ of the tanh function and the local coordinate r, which is defined based on the major radius coordinate. This r coordinate is used to remap the vertical $\mathrm{n_e}$ profile onto the LLAMA array. The Heaviside function ($\mathcal{H}$) splits the behavior of the density profile between the hyperbolic tangent tanh at the plasma edge and a linear function with a finite slope, $-m$ from the top of the pedestal inward. Each Thomson Scattering time slice is fitted with this tanh function, see Figure 5. The height of the pedestal, $\mathrm{n_{e,PED}}$, and the width of the pedestal, $\Delta \mathrm{n_e}$ synthesize the pedestal structure and can be leveraged to identify connections between

the pedestal and external factors, such as gas injection.

The heuristic measure for opaqueness depends not only on the pedestal density, but also the separatrix density. The separatrix density is not the base of the tanh and in the steep density region the separatrix density is sensitive to small variations in radial location of the separatrix. To reduce the variation in the spread of the electron density separatrix linked to magnetic equilibrium reconstruction we use power balance to determine the electron temperature and density at the separatrix.

The power crossing the last closed surface of magnetic flux can be estimated as

$$\mathrm{P_{LCFS}} = \mathrm{P_{Aux}} + \mathrm{P_{Ohmic}} - \mathrm{P_{rad,bulk}} - \mathrm{dW/dt} \tag{1}$$

where $\mathrm{P_{Aux}}$ is the total auxiliary heating power, $\mathrm{P_{Ohmic}}$ is the ohmic heating, $\mathrm{P_{rad,bulk}}$ is the power radiated in the bulk, and dW/dt is the time derivative of the stored energy W. In this work, we assume $dW/dt \sim 0$, corresponding to a quasi-steady inter-ELM state. This approximation is justified by the selection of stationary time windows in our database, which avoids phases with strong energy transients, specifically the pre-ELM phase (80-98%).

We note that although this assumption is common in separatrix power balance approximations, the dW/dt term can still represent a non-negligible fraction of the absorbed power during certain inter-ELM intervals, as shown in previous work [25–27]. For the analysis presented here, we assume that dW/dt $\sim$ 0 during the inter-ELM periods, consistent with the quasi-stationary profiles selected in our database. We note that this approximation may underestimate the separatrix power flux in specific time slices where the stored energy is still evolving. A dedicated study to resolve dW/dt systematically is left for future work. Therefore, the power balance equation simplifies to:

$$\mathrm{P_{LCFS}} = \mathrm{P_{Aux}} + \mathrm{P_{Ohmic}} - \mathrm{P_{rad,bulk}}. \tag{2}$$

To determine the position of the LCFS, we use the two-point model, which approximates the parallel heat flux, $q_{||}$, in the Scrape-Off Layer (SOL) with an analytic expression [28–30], similar to the approach by Spitzer and Härm in [31] for conductivity regimes. The Spitzer-Härm expression is given by:

$$q_{||}^{Spitzer} = 2\kappa_0 T_e^{7/2}/7L_{||}, \tag{3}$$

where κ_0 is the electron heat conductivity, and $L_{||}$ is the parallel connection length, approximated by $\pi\, R\, q_{95}$. The position of the separatrix can then be estimated using:

$$q_{||} = \frac{1/4\, P_{SOL}}{2\pi R \lambda_q} \frac{|B|}{B_p}, \tag{4}$$

where λ_q is the heat flux width and it is approximated using the scaling given in [32], R is the major radius, $|B|$ is the magnitude of the magnetic field, and B_p is the poloidal

DIII-D	$T_{e,SEP}$	$n_{e,SEP}$	$T_{e,PED}$	$n_{e,PED}$	$\Delta_{n_e}^{LFS}$	$\Delta_{n_e}^{HFS}$
	(eV)	(10^{19}m^{-3})	(eV)	(10^{19}m^{-3})	(cm)	(cm)
Min.	53.20	0.71	329	2.77	1.97	2.61
Max.	89	2.78	1559	10.32	10.63	17.44

Table 2: Electron density and temperature parameters.

component of the magnetic field. The poloidal magnetic field (B_p) is estimated using Ampère's law in a cylindrical approximation, incorporating a shaping parameter such as elongation (κ) based on [17], following approaches described in [28, 31, 33–36]. The Spitzer-Harm $q_{||}(r)$ [37], is integrated on the major radius axis from a r-coordinate to the wall until it matches the power crossing the separatrix, determining the electron temperature at the separatrix position, as described in [17, 32]. This is represented by:

$$P|_{r\,\to\,wall} = \frac{\mu_0 I_p}{aB_{T,center}R\sqrt{(1+\kappa^2)/2}} \int_r^{wall} r^2 q_{||}(r)dr, \quad \text{where} \tag{5}$$

$$\text{when} \quad P|_{r\,\to\,wall} = \frac{1}{4}P_{SOL}, \quad \Rightarrow \quad r = r_{SEP}.$$

Here, $B_{T,center}$ represents the toroidal magnetic field at the center of the plasma, and the factor $1/4 = 1/2 \times 1/2$ represents a correction factor, where the first $1/2$ accounts for equal splitting of the heat flux between the inboard and outboard divertor targets, and the second $1/2$ represents the reduction in upstream heat flux resulting from the distributed power input along the parallel connection length from the outer midplane to the divertor target, as discussed in [28]. Nevertheless, in other works, the second $1/2$ factor can represent the splitting of heat flux between the ion and electron channels [32]. As the TS measures both the electron temperature as well as the electron density profile, the tanh fits are shifted to align the electron temperature location at the separatrix with the temperature calculated using the two-point model method based on equation 5. The same shift is applied to the electron density to extract the electron density at the separatrix and the variation in the database of the separatrix electron temperature and density values is shown in table 2.

3.2. Thomson scattering electron density profile remap on LLAMA array

The width of the pedestal is a key parameter in estimating the effect of neutrals on plasma penetration. In DIII-D, electron density, and temperature profiles are provided by the Thomson Scattering (TS) diagnostic, which has a vertical array, as shown in Figure 1. However, the LLAMA diagnostic is positioned horizontally between the midplane and the X-point, as also indicated in Figure 1, covering both the Low-Field Side (LFS) and the High-Field Side (HFS).

Therefore, in this database, the strategy used is to remap the temperature and density profiles obtained from TS location onto the coordinate surfaces of $\rho^*_{poloidal}$

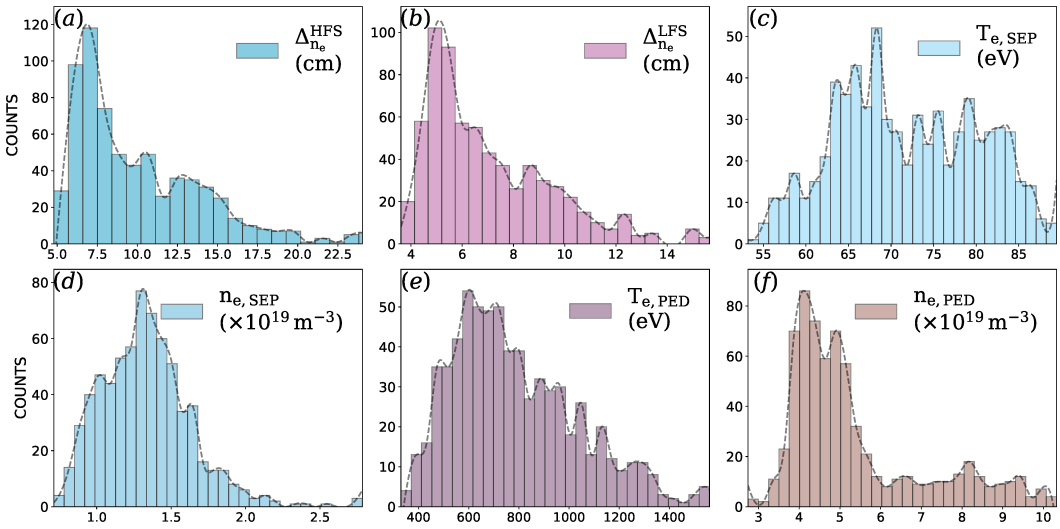

Figure 6: This figure highlights the histograms of the electron density and temperature profile parameters, including the pedestal height values, pedestal widths for the LFS and HFS, and the values of T_e and n_e at the separatrix.

at the location of the LLAMA diagnostic array. Due to this remapping technique, the scale of neutral penetration presented in this work is in centimeters (cm), which should be considered when comparing it with previous studies where usually the neutral penetration is estimated in (mm) because it is calculated at the outer mid-plane. However, this approximation of the electron density is subject to inaccuracies due to the poloidal asymmetry of electron density profiles, as discussed in [38–40]. Despite this limitation, it serves as a reasonable first-order approximation of n_e for estimating the neutral density (n_0). Under this approach, when mapping the electron density profile onto the LLAMA array, only a variation in pedestal width is observed compared to the original TS array, while the pedestal height remains unchanged. The spread in pedestal width on both the high field side and low field side at the location of the LLAMA is shown in figure 6.

3.3. Neutral parameters inference from the LLAMA diagnostic

Detailed measurements of the neutral density is crucial to estimate their influence on the pedestal structure. The new LLAMA diagnostic allows us to map the brightness of alpha decays in the Lyman band $\mathcal{B}_{\mathrm{Ly}_\alpha}$ radially [6, 7, 41–43]. The LLAMA measurements are tomographically inverted using the Abel inversion [44, 45] and Tikhonov regularisation [46] creating a radial profile of the emissivity on two arrays, one on the low-field side and the other on the high-field side, see figure (1) [6, 24]. The ionization rate profile is not obtained through direct diagnostics but is inferred from the reconstructed Lyman-alpha emissivity (ϵ_{Ly_α}). To estimate the local ionization rate S(r) and neutral density n_0(r), we combine ϵ_{Ly_α} with the measured electron temperature T_e(r), electron density n_e(r), and ion density n_i(r), using collisional–radiative rate coefficients from the

DIII-D	$n_{0,SEP}^{LFS}$	$\lambda_{n_0,SEP}^{LFS}$	$n_{0,SEP}^{HFS}$	$\lambda_{n_0,SEP}^{HFS}$
	$(10^{14}m^{-3})$	(cm)	$(10^{16}m^{-3})$	(cm)
Max.	28.5	2.9	4.4	3.4
Min.	1.64	0.8	0.42	0.4

Table 3: Summary of DIII-D LLAMA parameters dataset.

ADAS database [47]. Specifically, we use the photon emissivity coefficients (PEC) for excitation $PEC_{2\to1}^{exc}$ and recombination $PEC_{2\to1}^{rec}$, along with the effective ionization coefficient (SCD), to relate the observed emissivity to S(r) and $n_0(r)$ using standard expressions:

$$S = \frac{4\pi\epsilon_{Ly_\alpha} SCD_{2\to1}}{PEC_{2\to1}^{exc}} \tag{6}$$

$$n_0 = \frac{4\pi\epsilon_{Ly_\alpha} PEC_{2\to1}^{rec} n_i n_e}{PEC_{2\to1}^{exc} n_e} \tag{7}$$

The emissivity is expressed in units of photons $sr^{-1}m^{-3}s^{-1}$. In the pedestal region and deeper into the confined plasma (typically for $T_e > 100$ eV), the recombination contribution is negligible since $PEC_{2\to1}^{rec}$ is several orders of magnitude smaller than $PEC_{2\to1}^{exc}$. Furthermore, under such conditions, the ratio $SCD_{2\to1}/PEC_{2\to1}^{exc}$ is only weakly dependent on T_e and n_e, making the inferred ionization rate S(r) a particularly robust quantity [7].

Following the approach adopted in recent studies focused on the impact of neutral fueling on the pedestal structure [5,13], the neutral density profile is fitted with a simple exponential function (see figure 7).

$$n_0 = n_{0,SEP} \exp(\delta r/\lambda_{n_0}). \tag{8}$$

where $\delta r = r - r_{SEP}$, $n_{0,SEP}$ is the neutral density at the separatrix, and λ_{n_0} is the exponential decay length. This decay length represents the local neutral penetration depth at the separatrix location [2,15], see a summary of neutrals parameters in Figure (8). The fitting domain is restricted to the radial extent of the electron density pedestal, in the range of pedestal width, to provide a consistent and self-contained definition of λ_{n_0} at the separatrix and the resulting opaqueness $\eta = \Delta_{n_e}/\lambda_{n_0}$, in line with [5,13].

The neutral penetration length in this database for low-field side $\lambda_{n_0}^{LFS} \sim 0.8 - 2.9$ (cm) and high-field side $\lambda_{n_0}^{HFS} \sim 0.4 - 3.4$ (cm) is summarized in Table (3). The difference in the maximum values of λ_{n_0} between the HFS, $\lambda_{n_0}^{max} \sim 3.4$cm, and the LFS, $\lambda_{n_0}^{max} \sim 2.4$cm, suggests an additional resistance effect in the LFS compared to the HFS regarding neutral penetration. As indicated in [48] for MAST, it is highly likely that the pedestal in the LFS is associated with magnetic coordinates where the Shafranov shift causes a compression of flux surfaces, leading to higher densities and enhanced neutral attenuation in the LFS compared to the HFS. Consequently, neutrals would be more

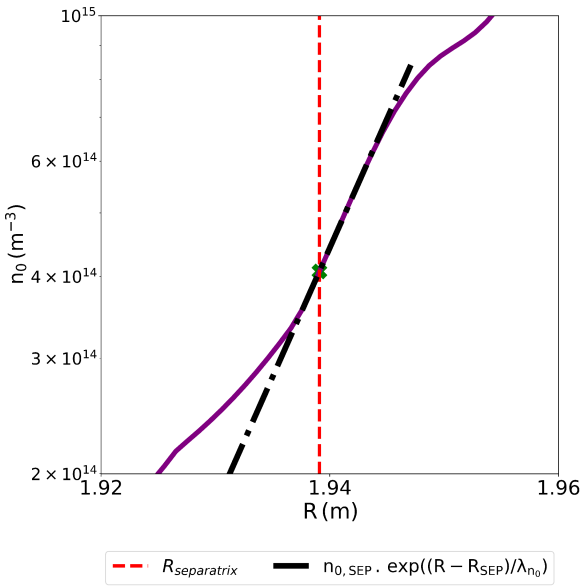

Figure 7: Radial profile of neutral density n_0 (purple solid line) from the LLAMA diagnostic array for DIII-D shot number 189337 @ time slice 4225.97 (ms). The red dotted vertical line represents the separatrix, the position where the neutral penetration depth is fitted with an exponential function tangential to the n_0 profile. This corresponds to the exponential fit shown on a logarithmic scale in this figure.

attenuated in the LFS than in the HFS, leading to a wider range of neutral penetration, $\Delta\lambda_{n_0}^{HFS} > \Delta\lambda_{n_0}^{LFS}$, with $\Delta\lambda_{n_0} = \lambda_{n0}^{max} - \lambda_{n0}^{min}$. This definition of $\Delta\lambda_{n_0}$ provides a more comprehensive representation of the variation across the entire database, as it captures the full range of values rather than relying on an isolated measurement of λ_{n_0}. This trend is consistent with the observations in the database. Regarding the minimum values of neutral penetration in both the HFS and LFS, these look like they are constrained by the resolution of the LLAMA diagnostic, $\sim$ 1cm. Nevertheless, most of these values are close to the diagnostic resolution but probably keep the physics dependencies between neutrals and the pedestal density. One of these physics dependencies is the neutral screening by the effect of the pedestal height as a reference.

3.4. Neutral penetration as function of pedestal height

The neutral penetration shows a decreasing trend over the range for $n_{e,PED} \sim 2.77 - 10.32\,(\times 10^{19} m^{-3})$ pedestal height as illustrated in Figure 9. The neutral penetration decreases both on HFS and LFS as pedestal density grows and saturates close to the spatial resolution of the LLAMA diagnostic, which is in the order of $1-2$ cm for LFS and HFS. Because the minimum values of λ_{n_0} are very close to the resolution limit of LLAMA ($\sim$ 1cm), their physical significance is limited but not negligible. For example, in the LFS, the values remain above the resolution limit, meaning that the decreasing trend of neutral penetration slows down but does not vanish, even as it approaches the resolution

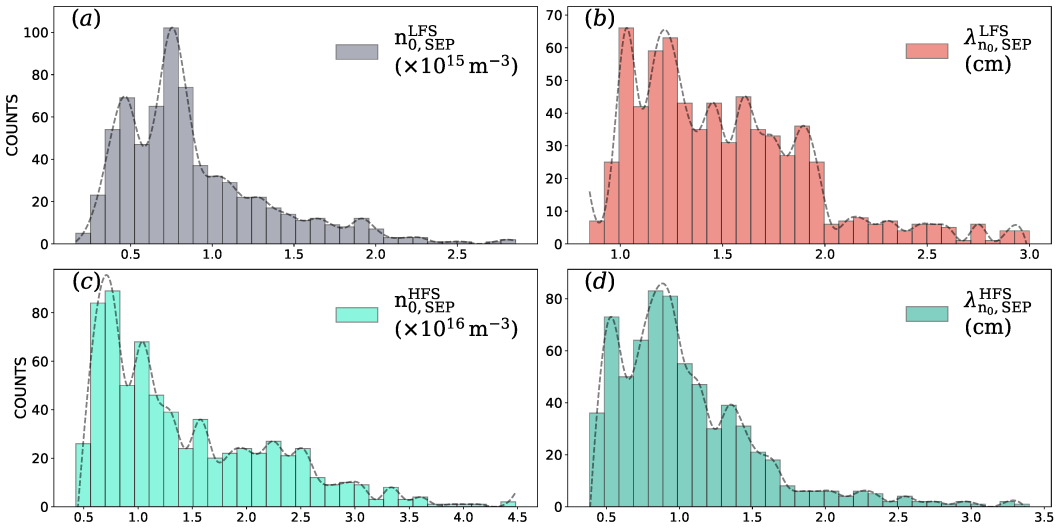

Figure 8: Histograms of neutral parameters inferred from LLAMA diagnostic. (a,c)The distributions of neutral density show an order-of-magnitude difference between the HFS and LFS, indicating stronger neutral attenuation in the LFS, likely influenced by ballooning transport, which is more significant in the LFS. (b,d) The neutral penetration values are consistent with the expected higher attenuation in the LFS.

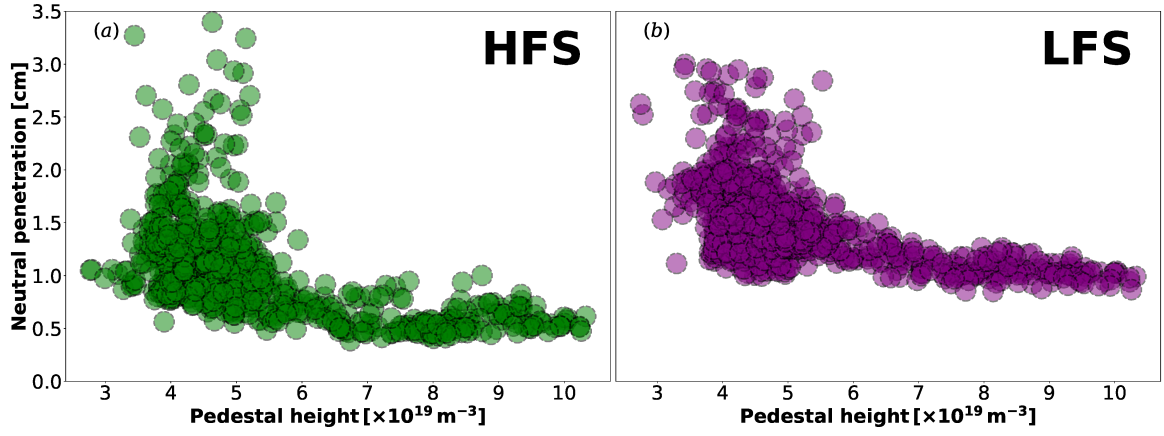

Figure 9: (a), (b) The penetration of neutrals decreases with a rising pedestal height, evidencing an effect known as "neutral screening". A certain minimum level for the penetration of neutrals is distinguished and is related to the resolution of the LLAMA diagnostic.

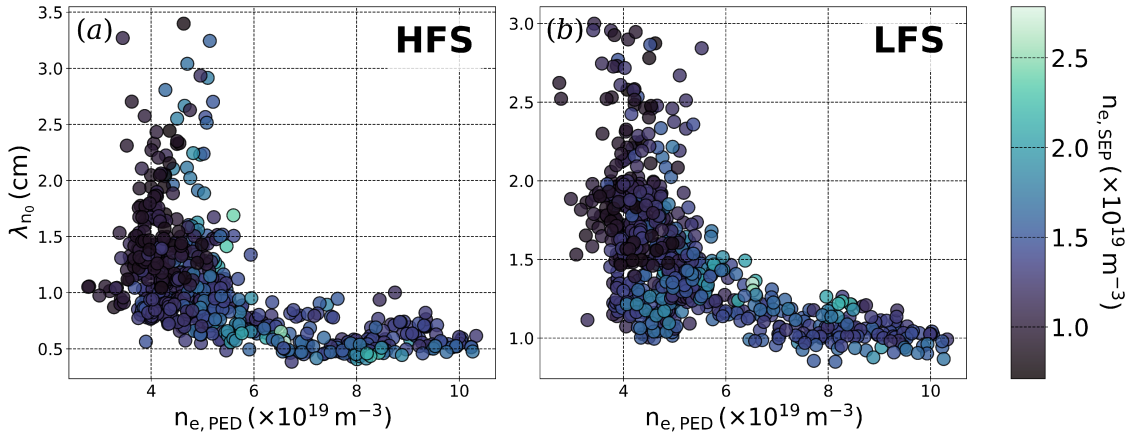

Figure 10: (a), (b) Neutral penetration length (λ_{rmn_0}) versus pedestal electron density ($n_{e,PED}$) for both the (a) High Field Side (HFS) and (b) Low Field Side (LFS). A colormap is applied to the scattered data points to represent the separatrix electron density ($n_{e,SEP}$). While an inverse correlation between λ_{n_0} and $n_{e,PED}$ has already been observed, this figure highlights that lower values of λ_{n_0}—associated with higher pedestal densities—also correspond to increased $n_{e,SEP}$, supporting the hypothesis that ionization is the dominant source of neutrals in these plasmas.

limit. Also, [5] reports an inverse relationship between λ_{n_0} and n_e, under the assumption that ionization is the dominant loss mechanism (sink) of neutrals. In this context, Figure (10) illustrates an increase in the separatrix electron density ($n_{e,SEP}$) as λ_{n_0} decreases, which is consistent with the ionization-dominant hypothesis. Nevertheless, the low-field side decay is very difficult to measure due to hollow emission profiles and this remark should be taken into account in future works for dedicated experiments.

For density values above $n_e \geq 6.0 \times 10^{19} m^{-3}$, which represents 55% of the total database, λ_{n_0} shows a slight saturation of neutrals for shallow penetrations. This effect is a direct consequence of the pedestal height being close to its maximum value, although it is not an exclusive factor. In the case of the HFS, the results are quite unexpected. Based on [48], penetration values should be lower in the LFS due to the effect of ballooning transport. However, they are actually lower in the HFS, suggesting that the role of the pedestal in neutral penetration changes for shallow penetrations and small values of λ_{n_0}. Another perspective suggests that the pedestal is not influenced solely by neutrals but also other mechanisms not considered in this study, such as turbulence driven transport. Recent works have demonstrated that turbulence, particularly electron temperature gradient (ETG) modes, can play a significant role in constraining the pedestal structure [49,50]. These turbulent processes may compete with neutral dynamics in shaping the pedestal evolution. At shallow neutral penetration values, these other factors become more relevant in the HFS, leading to an extraordinary attenuation of neutrals. As a result, penetration values in the HFS are lower than those observed in the LFS. This extended database over a wide range of plasma parameters

confirms the results of opaqueness experiments from C-Mod, which observed a similar trend of penetration depth versus pedestal height [15] (neutral screening effect). The database highlights that this observation is not just limited to the LFS, but also extends to the HFS, which was also observed in recent DIII-D and C-Mod modeling using SOLPS-ITER [5]. The key points to highlight from the present work, in comparison to the C-Mod study in [15] on the influence of gas puffing on pedestal profiles and the observed effect of "neutral screening," are as follows: Hughes *et al* in [15] used four plasma current ($I_p \in \langle 0.4, 0.6, 0.8, 1.0 \rangle$(MA)) values to enhance the Edge Transport Barrier (ETB) and consequently increase the pedestal height, allowing a comparison between puffed and unpuffed pedestal profiles for the same plasma current. The results in [15] show a greater effect of puffing when the plasma current and pedestal height are low, while for the maximum plasma current value, the variation in the pedestal due to puffing is imperceptible. Unlike the C-Mod study, the present database includes a wide range of pedestal height values independent of their associated plasma current. In this work, instead of comparing puffed and unpuffed profiles, a parameter (λ_{n_0}) is introduced to quantify the influence of neutrals, since the database contains a significantly larger number of samples than that of C-Mod. The influence of the pedestal over neutrals observed by comparing λ_{n_0} with the pedestal electron density, $n_{e,\mathrm{ped}}$, as shown in Figure (9), where an inverse dependence between λ_{n_0} and $n_{e,\mathrm{ped}}$ is evident, reaffirming the "neutral screening" effect reported in [15]. However, a key difference is observed in the conclusions regarding the effect of puffing (neutrals) in C-Mod and DIII-D. According to [15], the influence of puffing (neutrals) on the pedestal is relatively weak, whereas in the database analyzed in this work, the effect of neutrals is significant, and it is not negligible. The results shown in Figure (9) indicate that the variation in pedestal height (both in the HFS and LFS) from 3.0 to 6.0 ($\times 10^{19}\,\mathrm{m}^{-3}$), corresponding to a 100% increase, is associated with a decrease in λ_{n_0} from 3.5 cm to 0.5 cm in the HFS and from 3.0 cm to 1.0 cm in the LFS, representing a reduction in neutral penetration of 85% and 66%, respectively. Similarly, it is important to note that, although the influence of the pedestal over neutrals is a significant effect shown in this study, the scope of this work does not allow us to conclude that neutrals are exclusively or mainly attenuated by the pedestal.

4. Opaqueness of neutrals

The heuristic opaqueness metric indicates that the neutral penetration should be reduced as the pedestal density increases, as shown in the previous section. However, the heuristic model assumes that ionization is dominant and ignores any changes to the neutral density distribution and divertor conditions. In addition, the experimental opaqueness depends on the pedestal width, not the pedestal height and these are not necessary linked.

4.1. Experimental versus heuristic opaqueness

The inverse relationship between neutral penetration depth and pedestal density varies substantially as a function of device. While λ_{n_0} decreases with a higher pedestal density, on DIII-D the value is close $0.5-1$ cm for electron density values reach $1\times10^{20}\mathrm{m}^{-3}$, where on C-Mod these values are close to $2-5$ mm for $n_{e,PED}\sim2-4\times10^{20}\mathrm{m}^{-3}$ [2]. With a wide variety of magnetic fusion pilot plant concepts, there is a need to approximate the neutral fueling efficiency using a dimensionless quantity [1, 2, 5, 13, 24].

$$\eta=\frac{\Delta n_e}{\lambda_{n_0}} \tag{9}$$

η is the opaqueness and this is the ratio of Δn_e the electron pedestal width from the tanh fit and λ_{n_0} the neutral penetration depth from the exponential fits to the neutral density profile. If $\eta\sim1$ this means that the electron density pedestal and the neutral density profile have the same 'width'. However, if $\eta>1$ this means that the pedestal width is wider than the penetration depth of the neutrals, limiting the contributions of neutrals in determining the electron pedestal density structure. On the other hand, if $\eta<1$ the neutral density profile is wider than the electron density pedestal and the neutrals provide a large contribution to pedestal density structure.

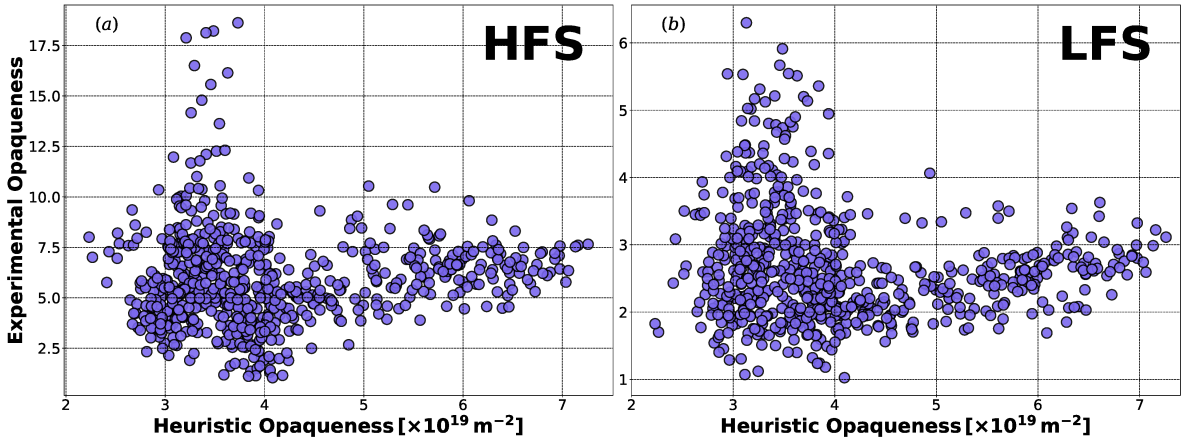

Figure 11: (a), (b) These figures for high-field and low-field sides compares the experimental opaqueness (η) with its heuristic approximation. Two distinct correlations are observed: a linear region for high average heuristic opaqueness values and a scattered region for low heuristic opaqueness values.

As the majority of devices don't have the capability to measure the neutral density profile inside the separatrix a heuristic approximation, $\eta^{Heur}\propto a\times n_e$, was developed to provide a quick approximation and predictive capability [1, 5]. Here a represents the minor radius of the plasma and the electron density approximation equal to $n_e=(n_{e,PED}+n_{e,SEP})/2$. Figure 11 shows that the experimental opaqueness increases with increasing heuristic opaqueness at high values. However, at low values, there is an

enormous spread in experimental opaqueness, whereas the heuristic opaqueness is low ($2.0 \times 10^{19}\mathrm{m}^{-2} \lesssim \eta^{\mathrm{Heur}} \lesssim 4.0 \times 10^{19}\mathrm{m}^{-2}$).

4.2. The influence of the ionization peak location

While the experimental and heuristic opaqueness are correlated at higher pedestal densities, this correlation breaks down at lower densities as shown in Figure 11. This suggests that additional factors influence the experimental opaqueness at lower electron density ($\mathrm{n_e}$) values, indicating a potential non-linear dependence of $\mathrm{n_e}$ on experimental opaqueness. The experimental opaqueness (η) represents the attenuation level of neutrals by the effect of the pedestal shape, particularly the width of the pedestal ($\Delta\mathrm{n_e}$). In future pilot plants, plasmas are expected to operate under high power injection conditions, with high pedestal density resulting in highly opaque plasmas.

In a high opaque scenario, the plasma will force the neutrals to ionize far from the pedestal, shifting the ionization peak towards the scrape-off layer as shown in Figure 12 [3]. Therefore, a plasma operating in a highly opaque scenario correlates with the position of the ionization peak in the scrape-off layer, with the peak moving further away from the pedestal zone (see Figure 12) in proportion to the plasma's increased opaqueness. We have extended this analysis to the present database, applying the same correlation logic to all opaqueness ranges, not just opaque plasmas.

Since we estimate the opaqueness η for the database and seek to unveil the dynamics followed by the position of the ionization peak† and its relation with the opaqueness level of the plasma, the present work seeks to compare experimental η with its heuristic approximation (η^{Heur}), which was explained in section (4.1), varying the position of the ionization peak and trying to evidence ranges of the opaqueness η that are correlated with a certain degree of closeness or remoteness of the ionization peak with respect to the pedestal. Thus, for certain degrees of closeness or remoteness of the ionization peak, the database gives an operational η range or a range for ionization peak position at which the experimental opaqueness takes its heuristic form. To facilitate generalization to other tokamaks, $\rho^*_{poloidal}$ (ρ^*_{pol}) coordinates ‡ are harnessed and a boundary between the pedestal zone and the scrape-off layer is estimated. To this end, we leverage the $\mathrm{r_{sym}}$ and $\Delta_{\mathrm{n_e}}$ parameters of the pedestal characterization process, assuming that $\Delta_{\mathrm{n_e}}$ encompasses the entire pedestal domain. Subsequently, the $\mathrm{r}^* = \mathrm{r_{sym}} + \frac{\Delta_{\mathrm{n_e}}}{2}$ coordinate, which coincides with the pedestal foot, is considered the boundary between the "pedestal region" and the scrape-off layer, as illustrated in Figure (13). As previously stated, our work is based on $\rho^*_{poloidal}$, so $\mathrm{r}^* = \mathrm{r_{sym}} + \frac{\Delta_{\mathrm{n_e}}}{2}$ is equivalent to $\rho^*_{pol}(\mathrm{r}^*) = \rho_{\mathrm{pedestal\,foot}}$. The parameter δ is calculated by first reconstructing the ionization profile using LLAMA measurements

†The LLAMA diagnostic usually measures two peaks of ionization on the HFS but for this work we just consider the peak most external.

‡$\rho^*_{poloidal}$ denotes the square root of the normalized poloidal magnetic flux, i.e., $\rho^*_{poloidal} = \sqrt{\psi_p/\psi_{p,sep}}$, where ψ_p is the poloidal magnetic flux and $\psi_{p,sep}$ is its value at the separatrix. This coordinate ranges from 0 at the magnetic axis to 1 at the separatrix and is widely used for radial profile comparisons [51]

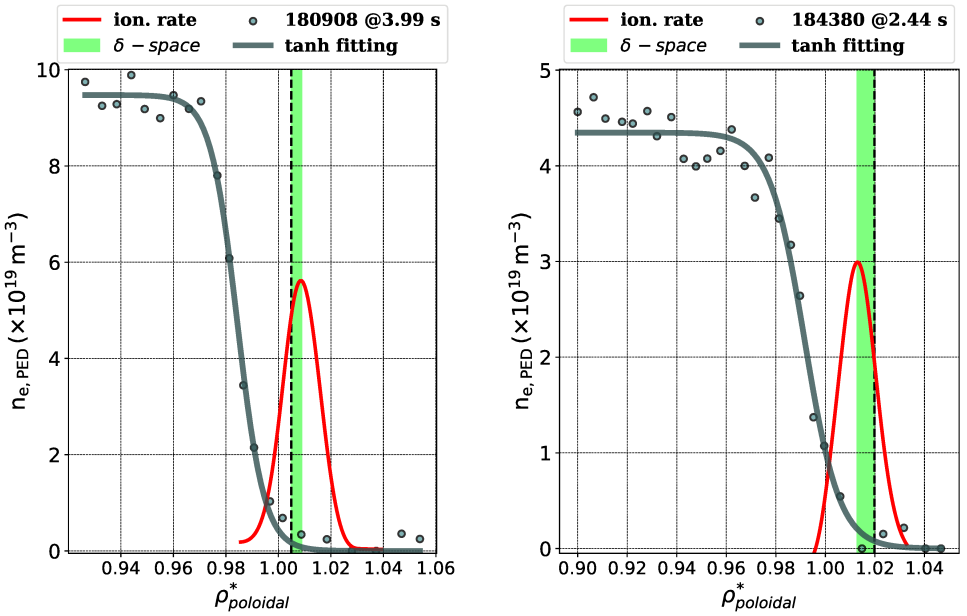

(a) Ionization peak in SOL (b) Ionization peak in pedestal region

Figure 12: This figure illustrates the position of the ionization peak (red solid line), identified via a local Gaussian fit around the maximum of the reconstructed ionization profile, relative to the pedestal foot position (black dotted line). The ionization profile shown corresponds to the one reconstructed from LLAMA measurements as described in [7]. The scales of the ionization profile are for illustration purposes, although the radial axis is physical. The highlighted green region, labeled as $\delta - space$, represents the distance δ between the ionization peak and the pedestal foot.

(see Equation 6), following the tomographic inversion procedure described in [7]. To identify the location of the ionization peak, a local Gaussian fit is applied around the maximum of the reconstructed profile. The peak of this fitted Gaussian is used solely to extract the position of maximum ionization, and it is then defined as the distance between this peak and the pedestal foot in $\rho^*_{poloidal}$ coordinate.

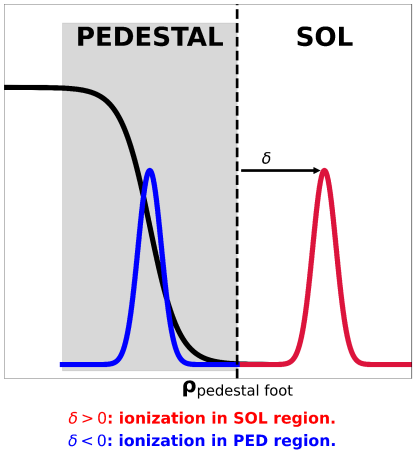

Figure 13: The following schematic illustrates the definition of the δ parameter, which indicates whether the ionization peak is situated within the scrape-off layer (SOL) or within the pedestal region.

Figures (15) illustrate that when the ionization is in the scrape-off layer ($\delta > -5.0 \times 10^{-3}$), both for the high-field and low-field sides, the experimental opaqueness assumes its heuristic form. Conversely, when the ionization peak is located in the "pedestal region," the experimental opaqueness dispersion on the low-field side is almost seven times ($\times 7$) larger (~ 17.5) than in the SOL region (~ 2.5), and the range of η^{Heur} is significantly reduced compared to the case with ionization in the SOL. Similarly, on the high-field side, the opaqueness dispersion in the pedestal region is three times ($\times 3$) higher (~ 6) than for SOL (~ 2), and the η^{Heur} range is also notably smaller. The results shown in Figures 15(a) demonstrate that the heuristic approximation of the opaqueness is a crucial tool for understanding opaque plasmas, particularly when the ionization peak is expected to be in the scrape-off layer. It is easy to observe in Figure 14 that the ionization peak is mainly located in the SOL region based on this database results.

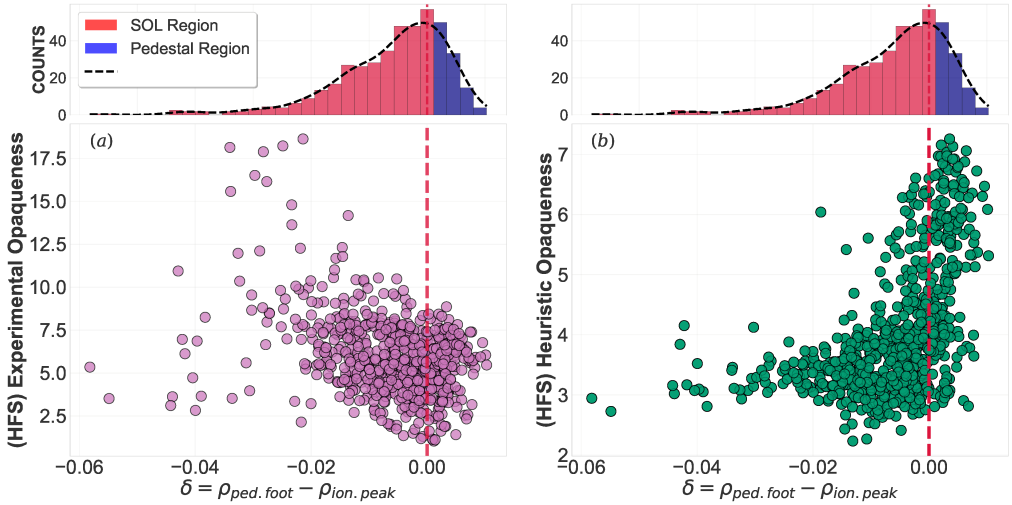

Figure 14: For discharges with the ionization peak in the scrape-off layer, the experimental opaqueness (a) shows a decrease as it approaches the pedestal foot. However, the heuristic opaqueness (b) shows a slight increase as it approaches the pedestal foot. When the ionization peak is in the SOL, there is no noticeable variation in the experimental opaqueness; on the contrary, the heuristic opaqueness increases rapidly.

The straightforward scaling of the heuristic approximation offers a valuable tool for developing scenarios in opaque plasmas, which will play a pivotal role in future fusion operations. Furthermore, the heuristic approach's relevance extends beyond merely describing opaque plasmas. It serves as a foundation for incorporating additional factors, such as the specific type and dominant isotope in the plasma, which has been extensively studied in [13] and validated across a broader sample space in this work.

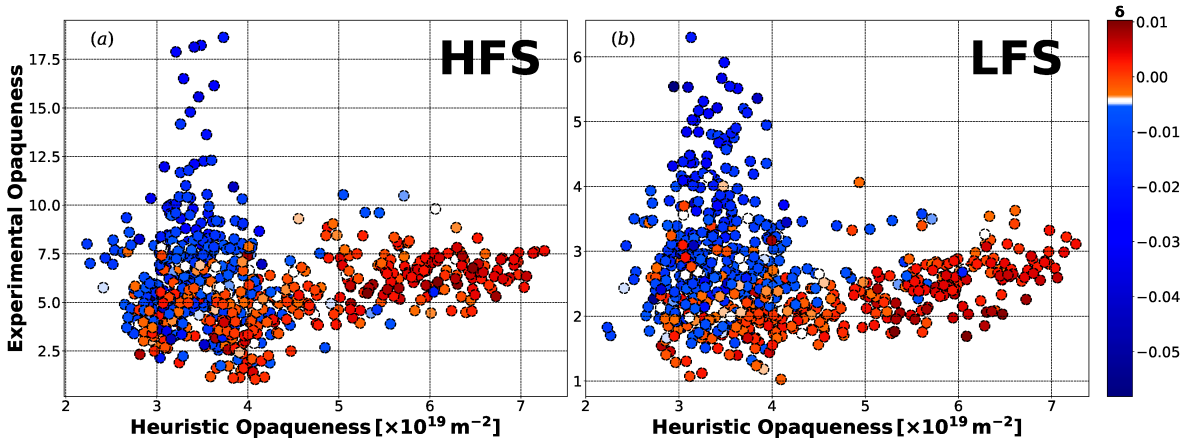

Figure 15: (a), (b) Comparison of the experimental opaqueness and the heuristic approximation. When the ionization peak is located inside the scrape-off layer (region in red) then the correlation between the opaquenesses is linear, Meanwhile the experimental opaqueness deviates from linear trend when the electron density is low and the ionization peak is inside pedestal (region in blue).

5. Conclusion and discussion

This work has generalized the neutral screening effect observed in C-Mod [15] to DIII-D and has corroborated the results of SOLPS simulations on C-Mod [2]. Thus, this work shows the screening on a DIII-D database and illustrates that opaque plasmas, as in future FPPs, will be characterized by plasmas with very high pedestal densities as indicated in [1]. Thus, the qualitative way to characterize how opaque a plasma is versus neutrals is by evidencing an inverse relationship between $\mathrm{n_{e,PED}}$ and $\lambda_{\mathrm{n_0}}$, as indicated in Figure (9). Independent of the tokamak scale, one way to quantify how opaque a plasma is is through the parameter η, defined as $\eta = \Delta_{\mathrm{ne}}/\lambda \mathrm{n_0}$, which allows us to estimate the degree of fueling efficiency. The present investigation reveals that η can be approximated heuristically [1,5] when the ionization peak lies in the scrape-off layer. Note that the ionization will lie mainly in the scrape-off layer when the pedestal density is high [2,15,16], and the opaqueness heuristic simplistically describes the dynamics of opaqueness for opaque plasma. Highlighting that η^{Heur} simplistically dominates opaque plasmas provides the opportunity to increase the complexity of the naïve model on the shoulders of the $\eta^{\mathrm{Heur}} \propto a \times \mathrm{n_e}$ expression, as has already been done for example in [13], $\eta^{\mathrm{Heur}} \sim a \times \sqrt{A} \times \mathrm{n_e}$, with targets in isotopic studies, being A the isotopes mass ratio.

However, the present work provides evidence supported by the results shown in Figures (15), which indicate that the opaqueness scale varies depending on the plasma region being studied (high-field side or low-field side). Observations in MAST highlight that the pedestal shape (height and width) is linked to geometrical coordinates when the pedestal is located on the high-field side [5,48]. In contrast, if the pedestal is located (measured) on the low-field side, it is instead linked to magnetic coordinates. This

finding underscores the relevance of ballooning transport on the low-field side, which manifests as an attenuation effect on the opaqueness level in this region. Consequently, an asymmetry emerges between the neutral penetration and the opaqueness of the high-field and low-field sides. In DIII-D, such asymmetry is observed, resulting in a relationship of $\eta^{\mathrm{HFS}} \approx 3 \times \eta^{\mathrm{LFS}}$, independently of the ionization peak position.

The above results highlight the relevance of opaqueness scaling in high-opaqueness scenarios, which are expected to dominate future experiments and machines such as ITER and SPARC. The usefulness of η_{Heur} lies in its ability to propose scenarios with a predetermined degree of opaqueness, allowing for better control over the fueling level. However, the opaqueness range described in this database is only valid for DIII-D, and additional studies are needed to extend this range to other machines. Furthermore, this database reflects the effect of fueling through recycling and gas puffing but does not account for alternative fueling strategies such as pellet injection. After being injected into the plasma, these pellets undergo ablation, generating two particle fluxes: one directed into the plasma and the other into the scrape-off layer. This process modifies the pedestal structure and, consequently, affects the opaqueness.

Another important point to emphasize is the strategy followed by LLAMA to infer the neutral density along its array [6], considering the different poloidal locations of the LLAMA and TS arrays, as shown in Figure (1). The remapping of the electron density profile should account for changes in pedestal width and height due to poloidal asymmetry effects, as reported in [38–40]. Consequently, these changes should also impact the derived neutral density profile. Therefore, using a Te and ne source located poloidally closer to the LLAMA array is expected to yield a more accurate estimation of the neutral density profile and, consequently, a more precise determination of the opaqueness. Finally, achieving such insights requires minimizing large-amplitude fluctuations in the pedestal parameters, which are more likely to occur in low-collisionality scenarios.

Acknowledgments

This material is based upon work supported by the U.S. Department of Energy, Office of Science, Office of Fusion Energy Sciences, using the DIII-D National Fusion Facility, a DOE Office of Science user facility, under Awards DE-FC02-04ER54698, DE-SC0019302, DE-SC0014264 and DE-AC02-09CH11466.

Disclaimer

This report was prepared as an account of work sponsored by an agency of the United States Government. Neither the United States Government nor any agency thereof, nor any of their employees, makes any warranty, express or implied, or assumes any legal liability or responsibility for the accuracy, completeness, or usefulness of any information, apparatus, product, or process disclosed, or represents that its use would

not infringe privately owned rights. Reference herein to any specific commercial product, process, or service by trade name, trademark, manufacturer, or otherwise does not necessarily constitute or imply its endorsement, recommendation, or favoring by the United States Government or any agency thereof. The views and opinions of authors expressed herein do not necessarily state or reflect those of the United States Government or any agency thereof.

References

[1] S. Mordijck. Overview of density pedestal structure: Role fueling versus transport. *Nucl. Fusion*, 60(8):082006, 2020.

[2] R. Reksoatmodjo, S. Mordijck, J.W. Hughes, J.D. Lore, and X. Bonnin. The role of edge fueling in determining the pedestal density in high neutral opacity Alcator C-Mod experiments. *Nucl. Mater. Energy*, 27:100971, 2021.

[3] A.L. Moser, A.W. Leonard, A.G. McLean, H.Q. Wang, and J.G. Watkins. The effect of divertor closure on detachment onset in DIII-D. *Nucl. Mater. Energy*, 19(3):67–71, 2019.

[4] A.C. Sontag, X. Cheng, J. Canik, A. Leonard, J.D. Lore, A.L. Moser, M. Murakami, J.M. Park, and C. Petty. Sol effects on the pedestal structure in DIII-D discharges. *Nucl. Fusion*, 57:076025, May 2017.

[5] S. Mordijck, R.A. Chaban, R. Reksoatmodjo, J.J. Balbin-Arias, Y. Chuang, J. Loughran, A.M. Rosenthal, M.A. Miller, T.M. Wilks, J.W. Hughes, F.M. Laggner, and T. Osborne. Impact of ionization and transport on pedestal density structure in DIII-D and alcator C-mod. *Nucl. Fusion*, 64(12):126034, 2024.

[6] A.M. Rosenthal, J.W. Hughes, A. Bortolon, F.M. Laggner, T.M. Wilks, R. Vieira, R. Leccacorvi, E. Marmar, A. Nagy, C. Freeman, and DIII-D Team. A 1D Lyman-alpha profile camera for plasma edge neutral studies on the DIII-D tokamak. *Rev. Sci. Instrum.*, 92(3):033523, 2021.

[7] A.M. Rosenthal, J.W. Hughes, F.M. Laggner, T. Odstrcil, A. Bortolon, T.M. Wilks, and F. Sciortino. Inference of main ion particle transport coefficients with experimentally constrained neutral ionization during edge localized mode recovery on DIII-D. *Nucl. Fusion*, 63:042002, 2023.

[8] F. Scotti, D.P. Stotler, R.E. Bell, B.P. LeBlanc, S.A. Sabbagh, V.A. Soukhanovskii, M.V. Umansky, and S.J. Zweben. Outer midplane neutral density measurements and H-mode fueling studies in NSTX-U. *Nucl. Fusion*, 61(3):036002, 2021.

[9] R.L. Boivin, J.A. Goetz, A.E. Hubbard, J.W. Hughes, I.H. Hutchinson, J.H. Irby, B. LaBombard, E.S. Marmar, D. Mossessian, C.S. Pitcher, and J.L. Terry. Effects of neutral particles on edge dynamics in Alcator C-Mod plasmas. *Phys. Plasmas*, 7(5):1919–1926, 2000.

[10] S. Potzel, M. Wischmeier, M. Bernert, R. Dux, F. Reimold, A. Scarabosio, S. Brezinsek, M. Clever, A. Huber, A. Meigs, and M. Stamp. Formation of the high density front in the inner far sol at asdex upgrade and jet. *Journal of Nuclear Materials*, 463:541–545, 2015. PLASMA-SURFACE INTERACTIONS 21.

[11] E. Stefanikova, L. Frassinetti, S. Saarelma, A. Loarte, I. Nunes, L. Garzotti, P. Lomas, F. Rimini, P. Drewelow, U. Kruezi, B. Lomanowski, E. de la Luna, L. Meneses, M. Peterka, B. Viola, C. Giroud, C. Maggi, and JET Contributors. Effect of the relative shift between the electron density and temperature pedestal position on the pedestal stability in JET-ILW and comparison with JET-C. *Nucl. Fusion*, 58:056010, Mar 2018.

[12] M G Dunne, S Potzel, F Reimold, M Wischmeier, E Wolfrum, L Frassinetti, M Beurskens, P Bilkova, M Cavedon, R Fischer, B Kurzan, F M Laggner, R M McDermott, G Tardini, E Trier, E Viezzer, M Willensdorfer, The EUROfusion MST1 Team, and The ASDEX-Upgrade Team. The role of the density profile in the asdex-upgrade pedestal structure. *Plasma Physics and Controlled Fusion*, 59(1):014017, oct 2016.

[13] R.A. Chaban, S. Mordijck, A.M. Rosenthal, M. Knolker, F.M. Laggner, T.H. Osborne, L. Schmitz,

K.E. Thome, and T.M. Wilks. The role of isotope mass on neutral fueling and density pedestal structure in the DIII-D tokamak. *Nucl. Fusion*, 64(4):046008, 2024.

[14] G.J. Wilkie, F. Laggner, R. Hager, A. Rosenthal, S.-H. Ku, R.M. Churchill, L. Horvath, C.S. Chang, and A. Bortolon. Reconstruction and interpretation of ionization asymmetry in magnetic confinement via synthetic diagnostics. *Nucl. Fusion*, 64(8):086028, Jun 2024.

[15] J.W. Hughes, B. LaBombard, D.A. Mossessian, A.E. Hubbard, J. Terry, T. Biewer, and Alcator C-Mod Team. Advances in measurement and modeling of the high-confinement-mode pedestal on the Alcator C-Mod tokamak. *Phys. Plasmas*, 13:056103, 2006.

[16] J.W. Hughes, B. LaBombard, J. Terry, A. Hubbard, and B. Lipschultz. Edge profile stiffness and insensitivity of the density pedestal to neutral fuelling in alcator C-Mod edge transport barriers. *Nucl. Fusion*, 47:1057–1063, Aug 2007.

[17] Bufferand H Ciraolo G. Balbin-Arias JJ, Bucalossi J and EUROfusion JET Team. Investigation of the dependency of JET midplane separatrix density as a function of engineering parameters. *Contrib. Plasma Phys.*, 60(5-6):e201900157, 2020.

[18] R.J. Groebner, D.R. Baker, K.H. Burrell, T.N. Carlstrom, J.R. Ferron, P. Gohil, L.L. Lao, T.H. Osborne, D.M. Thomas, W.P. West, J.A. Boedo, R.A. Moyer, G.R. McKee, R.D. Deranian, E.J. Doyle, C.L. Rettig, T.L. Rhodes, and J.C. Rost. Progress in quantifying the edge physics of the H mode regime in DIII-D. *Nucl. Fusion*, 41(12):1789–1805, 2001.

[19] D. Reiter, G.H. Wolf, and H. Kever. Burn condition, helium particle confinement and exhaust efficiency. *Nucl. Fusion*, 30(10):2141–2155, Dec 1990.

[20] G. Becker. Empirical scaling laws for local transport in neutral beam heated plasmas. *Nucl. Fusion*, 28(8):1458–1471, Aug 1988.

[21] R.J. Colchin, D.L. Hillis, R. Maingi, C.C. Klepper, and N.H. Brooks. The filterscope diagnostic on DIII-D. *Rev. Sci. Instrum.*, 74(3):2068–2071, 2003.

[22] S. Saarelma, A. Jarvinen, M. Beurskens, C. Challis, L. Frassinetti, C. Giroud, M. Groth, M. Leyland, C. Maggi, J. Simpson, and JET Contributors. The effects of impurities and core pressure on pedestal stability in joint european torus (JET). *Phys. Plasmas*, 22:056115, 2015.

[23] R.J. Groebner and S. Saarelma. Elements of h-mode pedestal structure. *Plasma Phys. Control. Fusion*, 65(7):073001, 2023.

[24] M.A. Miller, J.W. Hughes, S. Mordijck, M. Wigram, J. Dunsmore, R. Reksoatmodjo, and R.S. Wilcox. Particle control via cryopumping and its impact on the edge plasma profiles of alcator c-mod. *Nuclear Materials and Energy*, 42:101856, 2025.

[25] A.R. Field, I. Balboa, P. Drewelow, J. Flanagan, C. Guillemaut, J.R. Harrison, A. Huber, V. Huber, B. Lipschultz, and G. Matthews. Dynamics and stability of divertor detachment in H-mode plasmas on JET. *Plasma Phys. Control. Fusion*, 59(9):095003, 2017.

[26] A.R. Field, C.D. Challis, J.M. Fontdecaba, L. Frassinetti, L. Horvath, H.-T. Kim, C. Maggi, C.M. Roach, S. Saarelma, and M. Sertoli. The dependence of exhaust power components on edge gradients in JET-C and JET-ILW H-mode plasmas. *Plasma Phys. Control. Fusion*, 62(5):055010, 2020.

[27] D. Silvagni, O. Grover, A. Stagni, J.W. Hughes, M.A. Miller, B. Lomanowski, G. Ciraolo, M. Dunne, T. Eich, L. Frassinetti, C. Giroud, I. Jepu, A. Kallenbach, A. Kirjasuo, A. Kuang, T. Luda, C. Perez von Thun, T. Pütterich, H.J. Sun, and H. Zohm. The separatrix electron density in JET, ASDEX Upgrade and Alcator C-Mod H-mode plasmas: A common evaluation procedure and correlation with engineering parameters. *Nucl. Mater. Energy*, 42:101867, 2025.

[28] P. Stangeby. *The plasma boundary of magnetic fusion devices*. Institute of Physics Publishing, Bristol, UK, 2000.

[29] F. Nespoli, H. Bufferand, M. Valentinuzzi, N. Fedorczak, G. Ciraolo, E. Serre, Y. Marandet, R. Maurizio, H. De Oliveira, B. Labit, M. Komm, M. Faitsch, and S. Elmore. Application of a two-fluid two-point model to SOLedge2d-EIRENE simulations of TCV H-mode plasma. *Nucl. Mater. Energy*, 18:29–34, 2019.

[30] C. Wersal, P. Ricci, and J. Loizu. A comparison between a refined two-point model for the limited

tokamak SOL and self-consistent plasma turbulence simulations. *Plasma Phys. Control. Fusion*, 59:044011, 2017.

[31] Jr. Lyman Spitzer. *Physics of Fully Ionized Gases*. Interscience Publishers, New York, 1956.

[32] A.W. Leonard, A.G. McLean, M.A. Makowski, and P.C. Stangeby. Compatibility of separatrix density scaling for divertor detachment with H-mode pedestal operation in DIII-D. *Nucl. Fusion*, 57(8):086033, Jul 2017.

[33] M. Day, B. Merriman, F. Najmabadi, and R.W. Conn. The effect of heat flux limiting on divertor fluid models. *Contrib. Plasma Phys.*, 36(2-3):419–423, 1996.

[34] S.K. Erents, P.C. Stangeby, B. LaBombard, J.D. Elder, and W. Fundamenski. Simple relations between scrape-off layer parameters of high recycling divertors part i: The relation between 'upstream' density and temperature. *Nuclear Fusion*, 40(3):295, mar 2000.

[35] R. Cohen, L. Spitzer, and P.M. Routly. The electrical conductivity of an ionized gas. *Phys. Rev.*, 80(2):230–238, Apr 1950.

[36] L. Spitzer Jr and R. Harm. Transport phenomena in a completely ionized gas. *Phys. Rev.*, 89(5):977–981, Nov 1952.

[37] P.C. Stangeby, J.M. Canik, J.D. Elder, C.J. Lasnier, A.W. Leonard, D. Eldon, M.A. Makowski, T.H. Osborne, and B.A. Grierson. Identifying the location of the OMP separatrix in DIII-D using power accounting. *Nucl. Fusion*, 55(9):093014, Aug 2015.

[38] M. Groth, G.D. Porter, T.D. Rognlien, S. Wiesen, M. Wischmeier, M.N.A. Beurskens, X. Bonnin, B.D. Bray, S. Brezinsek, and N.H. Brooks. Poloidal distribution of recycling sources and core plasma fueling in DIII-D, ASDEX-Upgrade and JET L-mode plasmas. *Plasma Phys. Control. Fusion*, 53:124017, 2011.

[39] E.M. Hollmann, S. Brezinsek, N.H. Brooks, M. Groth, A.G. McLean, A.Yu. Pigarov, and D.L. Rudakov. Spectroscopic measurement of atomic and molecular deuterium fluxes in the DIII-D plasma edge. *Plasma Phys. Control. Fusion*, 48:1165–1184, 2006.

[40] A.A. Pshenov, A.S. Kukushkin, and S.I. Krasheninnikov. On detachment asymmetry and stability. *Phys. Plasmas*, 24:072508, 2017.

[41] A.M. Rosenthal, J.W. Hughes, F.M. Laggner, T. Odstrcil, A. Bortolon, T.M. Wilks, S. Mordijck, M.A. Miller, and F. Sciortino. Pedestal main ion particle transport inference through gas puff modulation with experimental source measurements. *Nucl. Fusion*, 64:036006, 2024.

[42] Ph. Mertens and M. Silz. Radial profiles of atomic deuterium measured in the boundary of TEXTOR 94 with laser-induced fluorescence. *J. Nucl. Mater.*, 241-243:842–847, 1997.

[43] D. Elliott, D. Sutherland, U. Siddiqui, E. Scime, C. Everson, K. Morgan, A. Hossack, B. Nelson, and T. Jarboe. Two-photon LIF on the HIT-SI3 experiment: Absolute density and temperature measurements of deuterium neutrals. *Rev. Sci. Instrum.*, 87:11E506, 2016.

[44] G.C.Y. Chan and G.M. Hieftje. Estimation of confidence intervals for radial emissivity and optimization of data treatment techniques in Abel inversion. *Spectrochim. Acta B*, 61:31–41, 2006.

[45] R.K. Paul. Novel approach to Abel inversion. *Rev. Sci. Instrum.*, 78:093701, 2007.

[46] M. Odstrcil, J. Mlynar, T. Odstrcil, B. Alper, A. Murari, and JET EFDA Contributors. Modern numerical methods for plasma tomography optimisation. *Nucl. Instrum. Methods Phys. Res. A*, 686:156–161, Sep 2012.

[47] H.P. Summers, W.J. Dickson, M.G. O'Mullane, N.R. Badnell, A.D. Whiteford, D.H. Brooks, J. Lang, S.D. Loch, and D.C. Griffin. Ionization state, excited populations and emission of impurities in dynamic finite density plasmas: I. the generalized collisional–radiative model for light elements. *Plasma Phys. Control. Fusion*, 48(2):263–293, 2006.

[48] A. Kirk, T. O'Gorman, S. Saarelma, R. Scannell, H.R. Wilson, and MAST Team. A comparison of H-mode pedestal characteristics in MAST as a function of magnetic configuration and ELM type. *Plasma Phys. Control. Fusion*, 51(6):065016, 2009.

[49] J.F. Parisi, D.R. Hatch, P.-Y. Li, J.W. Berkery, A.O. Nelson, S.M. Kaye, K. Imada, and M. Lampert. Turbulent transport-limited pedestals in tokamaks. Submitted to Phys. Plasmas,

2025.

[50] P.-Y. Li, D.R. Hatch, B. Chapman-Oplopoiou, S. Saarelma, C.M. Roach, M. Kotschenreuther, S.M. Mahajan, G. Merlo, and MAST Team. Etg turbulent transport in the mega ampere spherical tokamak (MAST) pedestal. *Nucl. Fusion*, 64(1):016040, 2024.

[51] J. Wesson. *Tokamaks*. Oxford University Press, Oxford, UK, 2nd edition, 1997.